

# Classification of same hand motor imagery using Riemannian Geometry and Recurrent Neural Network

Jacob Johansson

*School of Innovation, Design,  
and Engineering  
Mälardalen University  
Västerås, Sweden  
0009-0007-5439-3371*

Martin Ekström

*School of Innovation, Design,  
and Engineering  
Mälardalen University  
Västerås, Sweden  
0000-0003-4298-9550*

Elaine Astrand

*School of Innovation, Design,  
and Engineering  
Mälardalen University  
Västerås, Sweden  
0000-0002-3869-279X*

**Abstract**—Decoding imagery of different movements of the same limb from electroencephalogram data is challenging due to low signal-to-noise ratio and highly overlapping activation patterns. Here, we aimed to investigate whether Riemannian Geometry (RG) combined with Recurrent Neural Network (RNN) could be used to improve the decoding performance of hand open and close motor imagery. We evaluated our RG-RNN approach, using Area Under the Curve (AUC) metrics, in a population of 13 healthy subjects and compared it to Minimum Distance to Riemannian Mean and RG-Support Vector Machine. The RG-RNN approach outperformed the two other methods, achieving an average AUC of 0.65. These results suggest that RG-RNN offers a distinct advantage, likely due to its ability to capture temporal dependencies in the data, an aspect feasible due to the recurrent architecture of the network.

**Index Terms**—motor imagery, electroencephalography, Riemannian geometry, Recurrent Neural Network

## I. INTRODUCTION

Decoding imagery of different movements (motor imagery, MI) of the same limb from electroencephalogram (EEG) activity is important for the development of Brain-Computer Interface (BCI)-based rehabilitation after e.g. a stroke. Despite its clinical importance, only a small proportion of studies have focused on decoding same limb MI (only 3.5% in [1]). The majority of efforts have instead been put on distinguishing between MI of four body parts: tongue, left hand, right hand, and foot [2]. This is a substantially easier task as the EEG activation patterns are maximally separable from a neuroanatomical perspective.

Nonetheless, early studies have demonstrated the feasibility of decoding the same limb MI by using benchmarking feature extraction and classification methods (e.g. Common Spatial Patterns (CSP)-Linear Discriminant Analysis (LDA)/Support Vector Machine (SVM)), [3], [4]. Since then, the implementation of deep learning methods have improved the decoding further, showing promising performance on same limb decod-

ing tasks, with up to 73% accuracy for classifying open and close hand MI [5]–[7].

A parallel line of research has proposed the use of Riemannian Geometry (RG) in BCIs [8]. It is based on the use of covariance matrices that have typically been exploited by Principal Component Analysis (PCA) described in the Euclidean Geometric (EG) framework. However, covariance matrices are more naturally handled in the Riemannian manifold as it better describes their symmetric and positive definite (SPD) properties [8]. The first introduction of RG, applied on dataset IIa from the BCI competition IV, comprised of left/right hand, foot and tongue MI tasks, outperformed previous classification using CSP [9]. A recent study attempting to decode same limb motor intention of 6 different movements (including hand open and close) using a combination of source localization, RG, and SVM classification achieved 22.47% accuracy, which was 4.8% higher than using conventional filter bank-CSP [10]. Another previous study applying the RG framework to decode same-limb MI of 6 different classes (including open and close hand MI) achieved an impressive 80% accuracy [11]. Reproducing these results is necessary.

In this study, we aim at investigating whether combining RG and deep learning can better extract information of hand open (HO) and close (HC) MI. We have chosen a Recurrent Neural Network (RNN) for its ability to capture temporal structures in data and we compare it to Minimum Distance to Riemannian Mean (MDRM) and RG-based SVM classifiers.

## II. METHODS

### A. EEG recordings

Fifteen healthy right-handed participants aged from 22 to 53 years (average 31.4 years, 8 female participants) without prior experience of MI participated in this study. Two subjects were excluded from data analysis due to having misunderstood the instructions of the behavioral task. EEG recordings were carried out using 64 Ag/AgCl active electrodes (Brain Products, ActiCHamp). The electrodes were positioned according to the international 10/20 system. All electrode impedances

This work was funded through the Promobilia Foundation 18128, the Kamprad Family Foundation 20190119 and Mälardalen University.

were below 28kOhm during the full experiment. A total of 42 channels were selected for analysis and included: AFz, Fz, F1-4, FCz, FC1-6, Cz, C1-6, CPz, CP1-6, Pz, P1-6, POz, PO3-4, PO7-8, Oz, O1-2. We excluded eccentric channels due to the higher occurrence of artifacts at those locations. Sampling rate was kept at 1 kHz. During the experimental session, subjects sat comfortably in a chair facing a computer screen with their right lower arm in a fixed position to allow the hand to grasp around a wooden cylinder (diameter 3cm). The room was silent, and lighting was dimmed to avoid visual and auditory artifacts. Subjects were asked to relax and avoid unnecessary muscle and eye movements during the session. More details on the experimental condition can be found in [12]. All experimental procedures involving human subjects described in this paper were approved by the Ethical Review Board (Dnr. 2017/273/1), and participants gave written informed consent.

### B. Motor imagery task

Subjects were instructed to perform interleaved trials of Motor Execution (ME) and Motor Imagery (MI) of the right hand. Two movements were chosen, HC and HO including extension of fingers. For the scope of this article, only MI is analyzed here. A block consisting of one ME trial followed by one MI trial, started with the simultaneous presentation of a visual and an auditory instruction of which movement to perform (HO or HC). The visual instruction was presented for 4 seconds, after which a focus point (FP) appeared. Two seconds after the apparition of the FP, an auditory tone was played to mark task onset (i.e. instructing subjects to start performing the instructed task). Subjects were given 4 seconds to perform each task and were instructed to maintain their eyes open. Subjects performed two blocks with a total of 120 trials in randomized order during the experimental session (60 trials for each HO and HC).

### C. EEG preprocessing

To capture dynamic temporal characteristics of the data during each trial, a non-overlapping time window segmentation was implemented. One-second-long windows were chosen to balance the trade-off between temporal resolution, feature dimensionality, and signal quality. To address variations in the most informative frequency bands across individuals, filter banks were employed on the segmented data using a 4<sup>th</sup> order IIR Butterworth filter [13], [14]. The most relevant frequencies for each subject were identified by exploring a range of bandwidths defined as  $2^n \text{ Hz}$ ,  $n \in [0, \dots, 5]$ , with a step size of 2 Hz between 8 and 35 Hz, shown in Table I.

### D. Riemannian geometry

A Riemannian manifold,  $\mathcal{M}$ , is a differentiable manifold where every point on the manifold has a defined derivative and a homeomorphism mapping to a point in the neighbourhood of a reference point  $\mathbf{C} \in \mathcal{M}$ . The derivatives at a point on the manifold are the tangent space at that point [15]. Such a manifold is the space of symmetric positive definite

TABLE I  
FREQUENCY BANDS FOR EACH BANDWIDTH, WITH A 2 Hz STEP SIZE

Bandwidth	2 Hz	4 Hz	8 Hz	16 Hz	32 Hz
Freq. win. 1	8-10 Hz	8-12 Hz	8-16 Hz	8-24 Hz	8-35 Hz
Freq. win. 2	10-12 Hz	10-14 Hz	10-18 Hz	10-26 Hz	/
...	...	...	...	...	...
Freq. win. n	34-35 Hz	32-35 Hz	28-35 Hz	20-35 Hz	/

real matrices, which are defined as  $\{\mathbf{P} \mid \mathbf{P} \in \mathcal{M}, \mathbf{P}^T = \mathbf{P}, \mathbf{u}^T \mathbf{P} \mathbf{u} > 0, \forall \mathbf{u} \in \mathcal{R}^n\}$  [16]. Spatial covariance matrices belong to the class of symmetric positive definite matrices. For a given EEG signal trial  $\mathbf{x}_i \in \mathcal{R}^{C \times T_s}$ , where  $C$  is the number of channels,  $T_s$  number of samples per channel, and  $i$  is the  $i$ -th trial, the spatial covariance matrix (SCM) of  $\mathbf{x}_i$  is estimated by the unbiased sample covariance matrix  $\mathbf{C}_i \in \mathcal{R}^{C \times C}$  given by:

$$\mathbf{C}_i = \frac{1}{T_s - 1} (\mathbf{x}_i - \bar{\mathbf{x}}_i)(\mathbf{x}_i - \bar{\mathbf{x}}_i)^T \quad (1)$$

where  $\bar{\mathbf{x}}_i$  is the sample mean of the  $i$ -th trial [16]. These covariance matrices belong to the manifold space, making them incompatible with classifiers that expect input data to be in Euclidean vector space. To address this, each SCM is mapped as a vector-based feature by first projecting it onto the tangent space at the Riemannian mean of the SCMs, as described in [17], [18]. This projection is computed using the following equation:

$$\text{Log}_{\overline{\mathbf{C}}}(\mathbf{C}_i) = \overline{\mathbf{C}}^{\frac{1}{2}} \text{logm}(\overline{\mathbf{C}}^{-\frac{1}{2}} \mathbf{C}_i \overline{\mathbf{C}}^{-\frac{1}{2}}) \overline{\mathbf{C}}^{\frac{1}{2}} \quad (2)$$

where  $\text{logm}$  is the matrix logarithm [15]. Each projected SCM is then vectorized by the matrix vectorization operator  $\text{vec}: \mathcal{R}^{c \times c} \rightarrow \mathcal{R}^{c(c+1)/2}$  defined as:

$$\text{vec}(A) = [a_{11}, \sqrt{2}a_{12}, \sqrt{2}a_{13}, \dots, a_{22}, \sqrt{2}a_{23}, \dots, a_{CC}] \quad (3)$$

Where the scaling factor  $\sqrt{2}$  ensures that the Riemannian distance between the original SCMs is preserved in the tangent space, where the Euclidean norm is used. The Riemannian mean is computed iteratively for each class  $k \in \{1, \dots, K\}$  by

$$\overline{\mathbf{C}}_k = \arg \min_{\mathbf{C} \in \mathcal{M}} \sum_i \delta^2(\overline{\mathbf{C}}_{old}, \mathbf{C}_i) \quad (4)$$

where  $\delta^2(\overline{\mathbf{C}}_{old}, \mathbf{C}_i)$  is the Riemannian distance between the previous estimated Riemannian mean  $\overline{\mathbf{C}}_{old}$  and the manifold point  $\mathbf{C}_i$ , given by the inner product on the tangent space around  $\overline{\mathbf{C}}_{old}$  [17]

$$\delta^2(\overline{\mathbf{C}}_{old}, \mathbf{C}_i) = \text{trace}(\text{logm}(\overline{\mathbf{C}}_{old}^{-\frac{1}{2}} \mathbf{C}_i \overline{\mathbf{C}}_{old}^{-\frac{1}{2}})^2) \quad (5)$$

There is no closed-form solution for the Riemannian mean for more than two manifold points. Therefore, it is computed iteratively, shown in Algorithm 1

Where  $\|\cdot\|_F$  denotes the Frobenius norm operator,  $\epsilon$  is the threshold for the stopping criteria, and  $\text{Exp}_{\overline{\mathbf{C}}}$  maps the new estimated mean back to the manifold space using the matrix exponential operator [17]:

$$\text{Exp}_{\overline{\mathbf{C}}}(\mathbf{C}) = \overline{\mathbf{C}}^{\frac{1}{2}} \text{expm}(\overline{\mathbf{C}}^{-\frac{1}{2}} \mathbf{C} \overline{\mathbf{C}}^{-\frac{1}{2}}) \overline{\mathbf{C}}^{\frac{1}{2}} \quad (6)$$

---

**Algorithm 1** Riemannian Mean

---

```

Initialize  $\bar{\mathbf{C}} = \frac{1}{N} \sum_{i=1}^N \mathbf{C}_i$ 
while  $\left\| \frac{1}{N} \sum_{i=1}^N \text{Log}_{\bar{\mathbf{C}}}(\mathbf{C}_i) \right\|_F > \epsilon$ 
do

$$\bar{\mathbf{C}} \leftarrow \text{Exp}_{\bar{\mathbf{C}}} \left( \frac{1}{N} \sum_{i=1}^N \text{Log}_{\bar{\mathbf{C}}}(\mathbf{C}_i) \right)$$

end while

```

---

#### E. Feature extraction

The SCM for each frequency and time window is calculated using (1). Subsequently, the Riemannian mean,  $\bar{\mathbf{C}}_B$ , is calculated for each frequency window by aggregating the corresponding time window SCMs, as described in Algorithm 1. To extract Euclidean feature vectors, the SCMs are mapped to the tangent space at their respective Riemannian means using (2), vectorized with (3), and finally fused into a single feature vector.

For a single subject's EEG trial, the maximum number of features that can be extracted is

$$N_{\text{features}} = N_T \times N_B \times N_C(N_C + 1)/2 \quad (7)$$

where  $N_T$  is the number of time windows,  $N_B$  is the number of frequency bands, and  $N_C$  is the number of channels.

#### F. Feature dimension reduction

As the dimensionality of the extracted tangent space feature vectors significantly exceeds the limited number of trials, feature reduction is necessary to avoid overfitting [19]. To address this issue, partial least squares (PLS) regression was employed, as described in [18]. PLS maps, in a supervised manner, the original features and their corresponding labels into a new space where the covariance between them is maximized. Before applying PLS, all features were normalized to have a zero mean and unit standard deviation for each time window and frequency band to ensure consistency.

Various numbers of PLS components were tested and compared for evaluation. This process reduced the feature set to a maximum size equal to the selected number of PLS components:

$$N_{\text{features}} = N_{\text{plscomponents}} \quad (8)$$

#### G. Classification

Three different classifiers were implemented and tested to classify HO and HC MI: MDRM, SVM and an RNN. All classifiers utilized the RG method as feature extraction, but differed on the assumption of the space and sequence of the data. Specifically, MDRM operates directly in the manifold space while both SVM and RNN require the data to be in Euclidean vector space. The optimal parameters for each specific subject was identified by using a grid-search strategy.

For each classifier, the configuration with parameters resulting in the highest AUC score was labeled optimized, while the configuration with parameters resulting in the lowest AUC score was labeled non-optimized.

*a) MDRM:* MDRM operates directly on the manifold by computing the geodesic distance between two points on it. Classification is performed by evaluating the geodesic distance between the SCM,  $\mathbf{c}_{\text{class},i,W,B}$ , of a given trial and the class mean SCM,  $\bar{\mathbf{c}}_{\text{class},W,B}$ , for each time window and frequency band. The total distance for each class is then calculated as:

$$\delta_{\text{class}} = \sum_i \delta(\mathbf{c}_{\text{class},i,W,B}, \bar{\mathbf{c}}_{\text{class},W,B}) \quad (9)$$

where  $\mathbf{c}_{\text{class},i,W,B}$  represents the SCM of the  $i$ -th trial for the given class, time window  $\mathbf{W}$  and frequency window  $\mathbf{B}$ , and  $\bar{\mathbf{c}}_{\text{class},W,B}$  is the mean SCM of the corresponding class. Given that spatial information is embedded in the SCMs, the class with the minimum total geodesic distance is selected as the classification outcome.

During training, the intra-class Riemannian mean is computed for each class, time window, and frequency window using all training trials. This results in  $\mathbf{N}_W \times \mathbf{N}_B \times \mathbf{N}_K$  number of means per trial, where  $\mathbf{N}_W$  is the number of time windows,  $\mathbf{N}_B$  is the number of frequency bands, and  $\mathbf{N}_K$  is the number of classes. During inference, the average distance between the SCM of each new, unknown trial and the corresponding class means is calculated. The class with the minimum average distance determines the trial's classification.

*b) SVM:* Unlike MDRM, SVM expects the data to reside in Euclidean vector space. Each SCM,  $\mathbf{c}_{i,W,B}$ , representing the SCM for a specific time and frequency window, is mapped to the tangent space around its corresponding mean,  $\bar{\mathbf{c}}_{B,W}$ , vectorized into a feature vector, and processed using PLS for dimensionality reduction, as described in Sections II-E and II-F. A Radial Basis Function (RBF) kernel was chosen due to the non-linear separability of the data. The RBF kernel maps the data to a higher-dimensional space based on the distances between the data points, where the data are linearly separable, and identifies the decision boundary between them. For additional details, refer to [20].

The RBF kernel's performance depends on two parameters: gamma ( $\gamma$ ) and  $C$ . Gamma controls the influence of individual trials on the decision boundary, while  $C$  balances the trade-off between correctly classifying individual trials and maximizing the margin between classes. The optimal values for  $\gamma$  and  $C$  were determined using the grid-search strategy over the ranges  $\gamma \in [10^{-2}, 10^2]$ ,  $C \in [10^{-3}, 10^3]$ .

*c) RNN:* The RNN network consists of four distinct layers: an LSTM layer, a dropout layer, a linear layer, and a classification layer. Each layer is described below:

- **LSTM:** The Long short-term memory (LSTM) layer is a type of RNN designed to address the vanishing gradient problem, allowing it to handle long sequences of data. The LSTM layer has three key parameters:

- $\mathcal{L}$ : the number of layers,

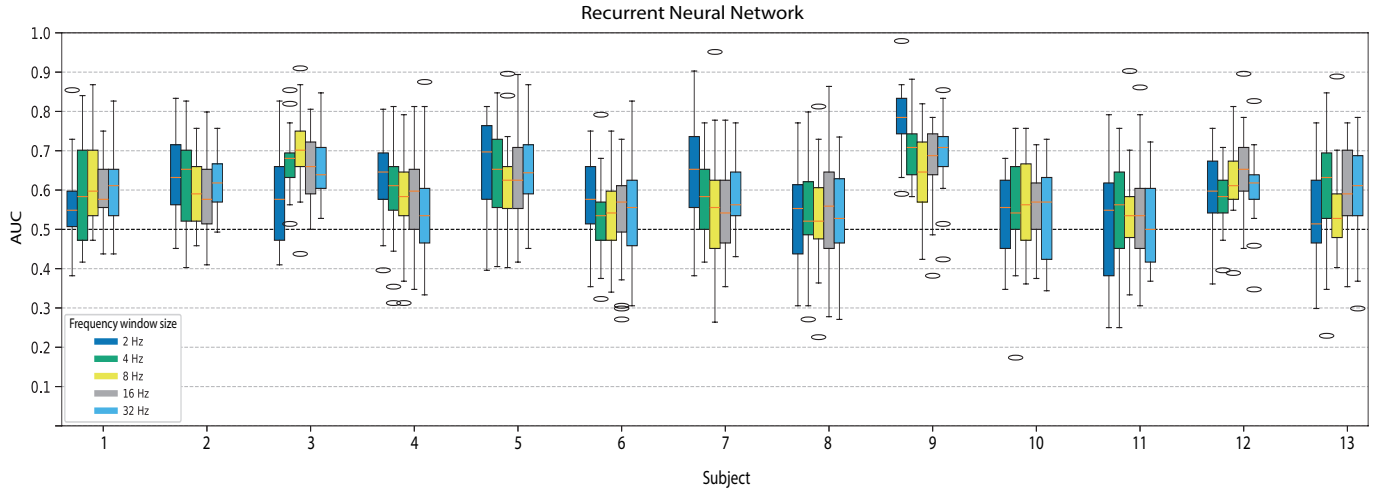


Fig. 1. Optimized RNN for each subject and frequency window size. Each bar represents AUC for each trial and cross-validation fold. Whiskers denote the range extending from the box to the farthest data point within 1.5 times the inter-quartile range.

- $\mathcal{H}$  the number of hidden units,
- $\mathcal{B}$  whether the LSTM is bidirectional.

A bidirectional LSTM was used, and the parameters were optimized using a grid-search strategy with the following ranges:  $\mathcal{L} \in \{1, 2, 4, 8, 16, 32, 64\}$ ,  $\mathcal{H} \in \{2, 4, 8, 16, 32, 64, 128\}$ .

- Dropout: The dropout layer regularizes the LSTM by reducing the risk of overfitting. It works by probabilistically excluding hidden units from activation and weight updates during the training of the network. Dropout probabilities of  $p_{dropout} \in [20\%, 40\%, 60\%]$  were explored.
- Linear: This layer flattens the output from the LSTM layer, preparing it for the classification layer.
- Classification: The classification layer uses a sigmoid activation function to compute the probability of belonging to each class.

Unlike SVM, which creates a decision boundary based on features aggregated over the entire three-second trial, the RNN is designed to capture temporal characteristics of the data. Consequently, the feature vector is constructed by concatenating features from each time window across all frequency windows. The resulting feature vector has the dimensionality of  $\mathcal{R}^{N_W \times N_{plscomponents}}$  per trial.

#### H. Evaluation

Given the high variability among subjects, the performance of each model was evaluated on a per-subject basis. A repeated 5-fold cross-validation approach with equal number of trials was used for each class. In this process, four folds were used for training and the remaining fold for testing. This procedure was repeated five times, rotating the test fold each time, so that every fold served as the test set exactly once.

Since the classification task is binary, Receiver Operating Characteristics (ROC) was used as the evaluation criteria,

with True Positive Rate (TPR) and False Positive Rate (FPR) serving as metrics. These metrics are defined as:

$$TPR = \frac{TP}{TP + FN} \quad (10)$$

$$FPR = \frac{FP}{FP + TN} \quad (11)$$

where  $TP$ ,  $FP$ ,  $TN$ , and  $FN$  represent the number of true positive, false positive, true negative, and false negative trials, respectively. For each fold, subject, and combination of hyperparameters, the Area Under the Curve (AUC) was computed for comparison between classifiers.

## III. RESULTS

### A. Subject variability and impact of frequency window size

To investigate the impact of frequency window sizes—and consequently the number of features per electrode—on the classification of hand open (HO) and hand close (HC) motor imagery (MI), we extracted input features using various frequency window sizes (see Methods). Substantial inter-subject variability was observed in terms of optimal frequency width (Fig. 1): 2 Hz ( $n = 5$  subjects), 4 Hz ( $n = 3$ ), 8 Hz ( $n = 1$ ), 16 Hz ( $n = 3$ ), and 32 Hz ( $n = 2$ ). Some subjects benefited from a specific frequency window size; for example, subject 9 showed significantly better AUC with the 2 Hz window. However, across all subjects, no overall improvement in AUC was found for any particular frequency window size (mean AUC across trials: 2 Hz =  $0.60 \pm 0.07$ , 4 Hz =  $0.60 \pm 0.05$ , 8 Hz =  $0.59 \pm 0.05$ , 16 Hz =  $0.59 \pm 0.05$ , 32 Hz =  $0.59 \pm 0.05$ ; one-way repeated measures ANOVA with frequency window size as main effect,  $p = 0.44$ ).

### B. Comparing MDRM, SVM and RNN

We investigated whether RNN could perform better than other more simple classification algorithms by comparing it

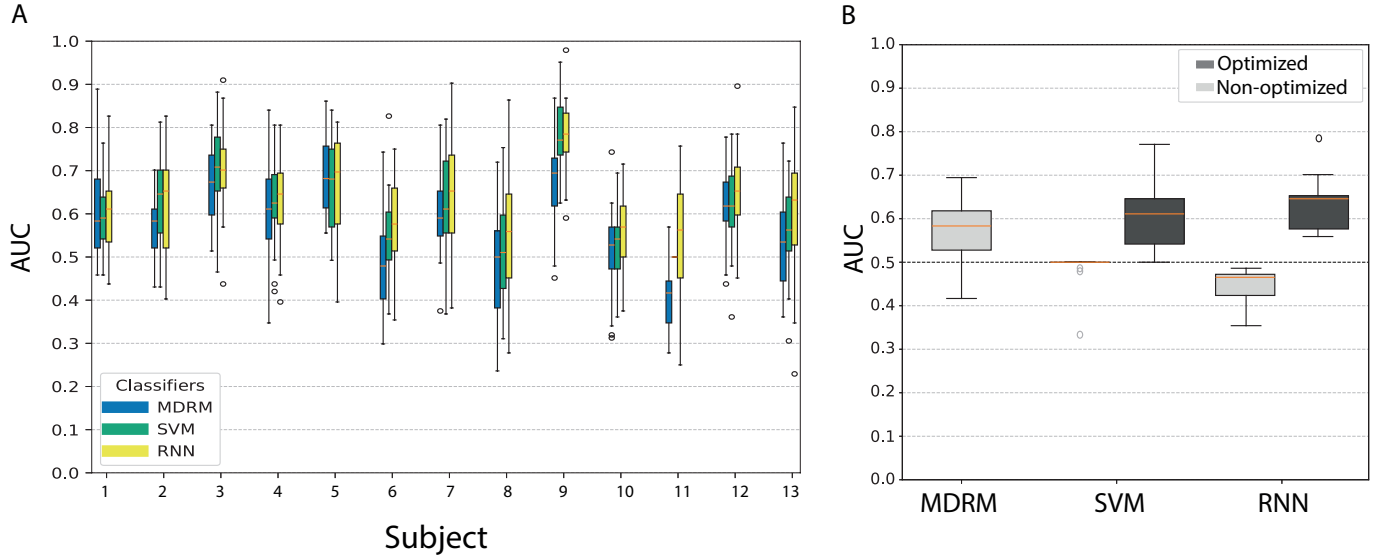


Fig. 2. (A) Comparison of optimized classifiers: MDRM, SVM, and RNN, highlighting the variability in performance across subjects for each classifier. (B) Comparison between non-optimized and optimized classifiers: MDRM, SVM, and RNN. Boxes represent AUC for each subject. The red line corresponds to the median and the whiskers represent the range extending up to 1.5 times the inter-quartile range from the first and third quartiles.

to the standard MDRM and commonly used SVM. All classifiers received RG-based features as described in the Methods section. As can be seen in Fig. 2A, the RNN performed systematically better on a subject level. On an aggregated level, it was significantly better than the SVM and MDRM (Fig. 2B; MDRM AUC=  $0.58 \pm 0.06$ ; SVM AUC=  $0.61 \pm 0.07$ , RNN AUC=  $0.65 \pm 0.05$ ; Wilcoxon non-parametric paired signrank test with Bonferroni correction for n=2 tests; MDRM vs. RNN p=0.000049, SVM vs. RNN p=0.0015). It can be further noted that it is necessary to optimize both the SVM and RNN, as the non-optimized versions of both could not discriminate between HO and HC MI (Fig. 2B).

#### IV. DISCUSSION

Classifying imagery of movements of the same hand from EEG data is a challenging task due to the inherent problem of volume conduction, which leads to low spatial resolution. We showed in a previous study with a portion of the same data (6 out of the 13 subjects) that extracting time-frequency features in the Euclidean space in combination with convolutional neural network (CNN) to classify HO and HC motor imagery, yielded an average accuracy of  $60.4\% \pm 0.85\%$  across the subjects [21]. In this study, we set out to investigate whether state-of-the-art RG for feature extraction in combination with deep learning could solve the task better. Comparing the exact same 6 subjects, the RG-RNN yielded  $60.3\% \pm 7.2\%$ . Although the average classification accuracy is similar, what can be noted is the large difference in variability between these two methods ( $0.85\%$  vs.  $7.2\%$ ). This indicates that there is a benefit of using RG-RNN for some subjects, possibly due to better spatial representation or presence of a temporal structure in the data for these subjects.

RG has rapidly grown and shown superior performance in EEG pattern decoding. Our results indicate that the RG framework can, in some subjects, better describe same-limb MI, and that, combined with RNN, performance can be improved. Our feature extraction pipeline, using the RG framework and applying PLS, is similar to that of Chu et al. (2020) [11]. However, our performance is not nearly in line with their accuracy, which may suggest possible methodological issues of overfitting in that study [11]. Another possible, explanation for this discrepancy, could be that Chu et al. had more EEG channels (64) in comparison to the 42 channels in our study. However, this is less likely as our channels were selected from a 64-channel system. Therefore, to what extent decoding same-limb MI from EEG-data is feasible using RG-based features needs to be further investigated.

Further, our results show that the RG-RNN performs slightly better than both MDRM and SVM, suggesting that some of the discriminative information between HO and HC motor imagery is encoded in the temporal structure of the EEG signals. We observed substantial inter-subject variability, with AUC values ranging from 0.56 to 0.79 for the RG-RNN. In addition to anatomical and measurement setup-related differences, this variability is likely amplified by the cognitively demanding nature of MI tasks, which inherently produce subject-specific neural patterns. Figure 1 and 2A illustrate this variability across subjects and classifiers: both SVM and MDRM exhibit similar variance (AUC standard deviations of 0.076 and 0.080, respectively), whereas RG-RNN demonstrates lower variance (AUC standard deviation of 0.063), indicating more stable performance. Notably, four subjects did not exceed an AUC of 0.6. However, the RG-RNN was uniquely capable of achieving above-chance performance for subject 11 (AUC = 0.56), where both MDRM and SVM failed to do so. This supports the

hypothesis that the temporal encoding of MI differs across individuals, which may explain the greater variability observed in RNN performance compared to other classifiers. Overall, the RG-RNN consistently outperformed the other methods, reinforcing its suitability for decoding same-limb MI across diverse subjects.

In this study, noise and artifacts were not specifically removed (using, e.g., independent component analysis or similar). As the quality of the EEG signals can substantially affect the efficacy of RG-based techniques, future work should implement robust artifact removal into the preprocessing pipeline. Additionally, the one-second long time windows used were uniform across all subjects. Optimizing these windows on a subject-specific basis could further enhance the performance of the model. Further, the sample size of this paper was constrained to 13 healthy participants and focused on subject-based optimization. A further study on a broader population could highlight the inter-participant differences even further. This paper was limited to healthy participants, continued research is needed to evaluate the proposed method on individuals with neurological impairments, e.g. after stroke. Moreover, new interesting directions are emerging, truly combining the RG framework with deep learning by embedding it into the structure of the deep neural network [22]. These advancements should also be explored in the context of MI decoding from EEG data.

## V. CONCLUSION

In this study, we explored the benefit of combining Riemannian geometry and a recurrent neural network for classifying hand open and close motor imagery from EEG data. We showed that the combination performed systematically (on a subject-level) better than the combination of RG with the simpler classification algorithms: MDRM and SVM.

These results highlight the complexity of decoding same-limb MI from EEG signals and the potential of leveraging temporal dynamics through recurrent architectures. The observed performance gains suggest that the RG-RNN framework can effectively capture and exploit the temporal structure in the EEG data during MI of same-limb HO and HC movements.

## REFERENCES

- [1] A. Al-Saegh, S. A. Dawwd, and J. M. Abdul-Jabbar, "Deep learning for motor imagery eeg-based classification: A review," *Biomedical Signal Processing and Control*, vol. 63, p. 102172, 2021. [Online]. Available: <https://www.sciencedirect.com/science/article/pii/S1746809420303116>
- [2] F. Lotte, M. Congedo, A. Lécuyer, F. Lamarche, and B. Arnaldi, "A review of classification algorithms for eeg-based brain-computer interfaces," *Journal of Neural Engineering*, vol. 4, no. 2, p. R1, jan 2007. [Online]. Available: <https://dx.doi.org/10.1088/1741-2560/4/2/R01>
- [3] P. Ofner, A. Schwarz, J. Pereira, and G. R. Müller-Putz, "Upper limb movements can be decoded from the time-domain of low-frequency eeg," *PLOS ONE*, vol. 12, no. 8, pp. 1–24, 08 2017. [Online]. Available: <https://doi.org/10.1371/journal.pone.0182578>
- [4] A. Suwannarat, S. Pan-ngum, and P. Israsena, "Comparison of eeg measurement of upper limb movement in motor imagery training system," *BioMedical Engineering OnLine*, vol. 17, p. 103, 08 2018. [Online]. Available: <https://doi.org/10.1186/s12938-018-0534-0>
- [5] R. Alazrai, M. Abuhijleh, H. Alwanni, and M. I. Daoud, "A deep learning framework for decoding motor imagery tasks of the same hand using eeg signals," *IEEE Access*, vol. 7, pp. 109 612–109 627, 2019.
- [6] N. Mammone, C. Ieracitano, and F. C. Morabito, "A deep cnn approach to decode motor preparation of upper limbs from time-frequency maps of eeg signals at source level," *Neural Networks*, vol. 124, pp. 357–372, 2020. [Online]. Available: <https://www.sciencedirect.com/science/article/pii/S089360802030037X>
- [7] W. Qiu, B. Yang, J. Ma, S. Gao, Y. Zhu, and W. Wang, "The paradigm design of a novel 2-class unilateral upper limb motor imagery tasks and its eeg signal classification," in *2021 43rd Annual International Conference of the IEEE Engineering in Medicine & Biology Society (EMBC)*, 2021, pp. 152–155.
- [8] M. Congedo, A. Barachant, and R. B. and, "Riemannian geometry for eeg-based brain-computer interfaces: a primer and a review," *Brain-Computer Interfaces*, vol. 4, no. 3, pp. 155–174, 2017. [Online]. Available: <https://doi.org/10.1080/2326263X.2017.1297192>
- [9] A. Barachant, S. Bonnet, M. Congedo, and C. Jutten, "Classification of covariance matrices using a riemannian-based kernel for bci applications," *Neurocomputing*, vol. 112, pp. 172–178, 2013, advances in artificial neural networks, machine learning, and computational intelligence. [Online]. Available: <https://www.sciencedirect.com/science/article/pii/S0925231213001574>
- [10] M. Zhang, J. Huang, and S. Ni, "Recognition of motor intentions from eegs of the same upper limb by signal traceability and riemannian geometry features," *Frontiers in Neuroscience*, vol. Volume 17 - 2023, 2023.
- [11] Y. Chu, X. Zhao, Y. Zou, W. Xu, G. Song, J. Han, and Y. Zhao, "Decoding multiclass motor imagery eeg from the same upper limb by combining riemannian geometry features and partial least squares regression," *Journal of Neural Engineering*, vol. 17, no. 4, p. 046029, aug 2020. [Online]. Available: <https://dx.doi.org/10.1088/1741-2552/aba7cd>
- [12] J. Tidare, M. Leon, and E. Astrand, "Time-resolved estimation of strength of motor imagery representation by multivariate eeg decoding," *Journal of Neural Engineering*, vol. 18, no. 1, p. 016026, feb 2021. [Online]. Available: <https://dx.doi.org/10.1088/1741-2552/abd007>
- [13] H. Fang, J. Jin, I. Daly, and X. Wang, "Feature extraction method based on filter banks and riemannian tangent space in motor-imagery bci," *IEEE Journal of Biomedical and Health Informatics*, vol. 26, no. 6, pp. 2504–2514, 2022.
- [14] A. M. Kristanto, E. C. Djamal, and R. Ilyas, "Motor imagery recognition using filter bank common spatial pattern and recurrent neural networks," in *2024 11th International Conference on Electrical Engineering, Computer Science and Informatics (EECSI)*, 2024, pp. 45–50.
- [15] O. Tuzel, F. Porikli, and P. Meer, "Pedestrian detection via classification on riemannian manifolds," *IEEE Transactions on Pattern Analysis and Machine Intelligence*, vol. 30, no. 10, pp. 1713–1727, 2008.
- [16] A. Barachant, S. Bonnet, M. Congedo, and C. Jutten, "Multiclass brain-computer interface classification by riemannian geometry," *IEEE Transactions on Biomedical Engineering*, vol. 59, no. 4, pp. 920–928, 2012.
- [17] J. Shin and W. Chung, "Multi-class motor imagery classification using multi-class svm with multi-band riemannian tangent space mapping," in *2023 11th International Winter Conference on Brain-Computer Interface (BCI)*, 2023, pp. 1–5.
- [18] Y. Chu, X. Zhao, Y. Zou, W. Xu, G. Song, J. Han, and Y. Zhao, "Decoding multiclass motor imagery eeg from the same upper limb by combining riemannian geometry features and partial least squares regression," *Journal of Neural Engineering*, vol. 17, no. 4, p. 046029, aug 2020. [Online]. Available: <https://dx.doi.org/10.1088/1741-2552/aba7cd>
- [19] E. Keogh and A. Mueen, "Curse of dimensionality," in *Encyclopedia of Machine Learning and Data Mining*, C. Sammut and G. I. Webb, Eds. Springer US, 2017, pp. 314–315.
- [20] M. Awad and R. Khanna, *Support Vector Machines for Classification*. Berkeley, CA: Apress, 2015.
- [21] J. Tidare, M. Leon, N. Xiong, and E. Astrand, "Discriminating eeg spectral power related to mental imagery of closing and opening of hand," in *2019 9th International IEEE/EMBS Conference on Neural Engineering (NER)*, 2019, pp. 307–310.
- [22] L. Dubreil, S. Labsir, E. Rouanet-Labé, and G. Pages, "Recurrent neural networks modelling based on riemannian symmetric positive definite manifold," in *2024 32nd European Signal Processing Conference (EUSIPCO)*, 2024, pp. 1192–1196.